

The role of crustal quartz in controlling Cordilleran deformation

Anthony R. Lowry¹ & Marta Pérez-Gussinyé²

¹Department of Geology, Utah State University, Logan, Utah 84322-4505, USA.

²Department of Earth Sciences, Royal Holloway, University of London, Egham, Surrey TW20 0EX, UK.

Large-scale deformation of continents remains poorly understood more than 40 years after the plate tectonic revolution¹. Rock flow strength and mass density variations both contribute to stress, so both are certain to be important, but these depend (somewhat nebulously) on rock type, temperature and whether or not unbound water is present². Hence, it is unclear precisely how Earth material properties translate to continental deformation zones ranging from tens to thousands of kilometres in width, why deforming zones are sometimes interspersed with non-deforming blocks and why large earthquakes occasionally rupture in otherwise stable continental interiors. An important clue comes from observations that mountain belts and rift zones cyclically form at the same locations despite separation across vast gulfs of time³ (dubbed the Wilson tectonic cycle), accompanied by inversion of extensional basins⁴ and reactivation of faults and other structures formed in previous deformation events⁵. Here we show that the abundance of crustal quartz, the weakest mineral in continental rocks², may strongly condition continental temperature and deformation. We use EarthScope seismic receiver functions⁶, gravity and surface heat flow measurements⁷ to estimate thickness and seismic velocity ratio, v_p/v_s , of continental crust in the western United States. The ratio v_p/v_s is relatively insensitive to temperature but very sensitive to quartz abundance^{8,9}. Our results demonstrate a surprising correlation of low crustal v_p/v_s with both higher lithospheric temperature and deformation of the Cordillera, the mountainous region of the western US. The most plausible explanation for the relationship to temperature is a robust dynamical feedback, in which ductile strain first localizes in relatively weak, quartz-rich crust, and then initiates processes that promote advective warming, hydration and further weakening. The feedback mechanism proposed here would not only explain stationarity and spatial distributions of deformation, but also lend insight into the timing and distribution of thermal uplift¹⁰ and observations of deep-derived fluids in springs¹¹.

Separating thermal and compositional influences on lithospheric rheology, understanding the roles of crust and mantle in lithospheric stability, and explaining structural reactivation and the Wilson tectonic cycle are among the primary goals of EarthScope¹, a major research equipment initiative to illuminate solid Earth processes using dense seismic and geodetic arrays. EarthScope's transportable seismic array has collected data at more than 1,000 sites and will eventually sample the entire continental United States at ~70-km spacing.

Compressional (v_p) and shear (v_s) seismic velocity fields are somewhat ambiguous tools for separating compositional variations from thermal effects, because they are sensitive to both. However, the ratio v_p/v_s is very sensitive to compositional variations in crustal rocks, and particularly the silica content (Fig. 1a, after ref. 8). Weighted regression of density versus v_p/v_s for continental rock types tracks the line from granite to gabbro, the silicic and mafic end-members of continental crystalline rocks. Variation in v_p/v_s for a large range of temperature⁹ is comparatively small. Inspection of v_p/v_s for constituent minerals (Fig. 1b) reveals that rock compositional dependence predominantly reflects sensitivity to quartz, because mafic minerals

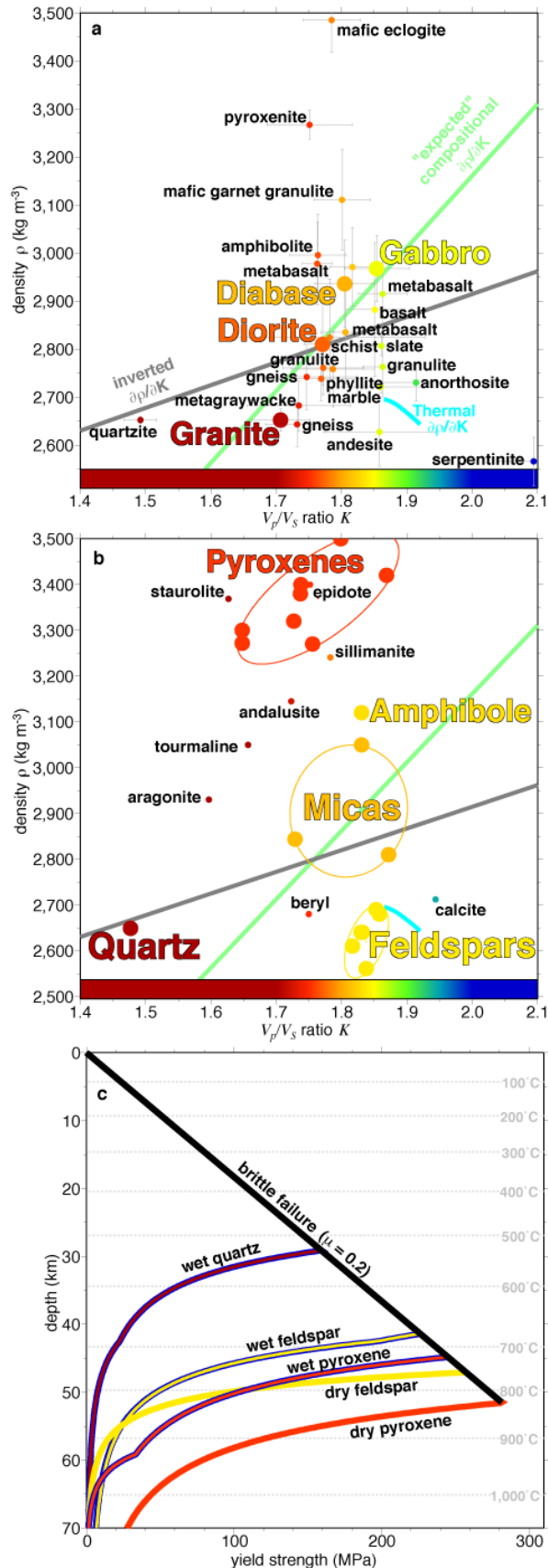


exhibit v_p/v_s that is similar to (or slightly lower than) feldspar and mica, the other major constituents of granite.

Figure 1. Laboratory measurements of rock properties. **a**, Density ρ versus velocity ratio v_p/v_s for rocks⁸; bars are 1σ . Green line is a weighted regression of laboratory measurements; grey line depicts slope inverted from geophysical data (see Methods). Cyan curve shows feldspar temperature dependence for a 20–900 °C range⁹; other minerals behave similarly. **b**, Density versus v_p/v_s for minerals⁸ shows quartz dominates the compositional relationship. **c**, Flow strength for crustal mineral constituents², assuming 10^{-14} s^{-1} strain rate, 1 mm grain size, and a geotherm from the Colorado plateau. Brittle-field failure assumes a frictional coefficient $\mu = 0.2$. Temperature, quartz abundance and water fugacity determine whether the lower crust flows.

A geophysical tool for mapping quartz concentration in crustal rocks would illuminate crustal deformation processes, because flow strength of crustal rocks is also sensitive to quartz. Mineral flow strength² for the lesser of dislocation and diffusion creep is shown in Fig. 1c; the strength of mineral constituents bounds that of rock aggregates (and weaker constituents are favoured). Hence the key factors influencing flow viscosity are temperature, water fugacity and abundance of quartz.

The ratio v_p/v_s is not widely used to estimate crustal composition because accurate estimation is difficult. Body wave tomograms, for example, often have very different path sampling for shear and compressional waves. Receiver-function studies of differences in P- and mode-converted S-wave arrival times from the Moho are sensitive to both crustal thickness (H) and v_p/v_s (K), so both can be estimated from amplitude stacks of seismic arrivals at times predicted for a range of possible H and K (ref. 12). However, v_p/v_s is poorly determined in receiver-function analyses when crustal depths are aliased, so it is commonly treated as a nuisance parameter if seismometer spacing exceeds a few tens of kilometres. Indeed, EarthScope Automated Receiver Survey (EARS⁶) estimates of v_p/v_s behave very much like random noise (Fig. 2a and c). An example

H - K parameter stack from Nevada (Fig. 2d) illustrates some of the problems: stack amplitude maxima are elongate in the K dimension, and real-Earth violation of the method's implicit assumptions (a one-dimensional medium with a single impedance contrast) results in smearing of stacked phase arrival energy and multiple maxima.

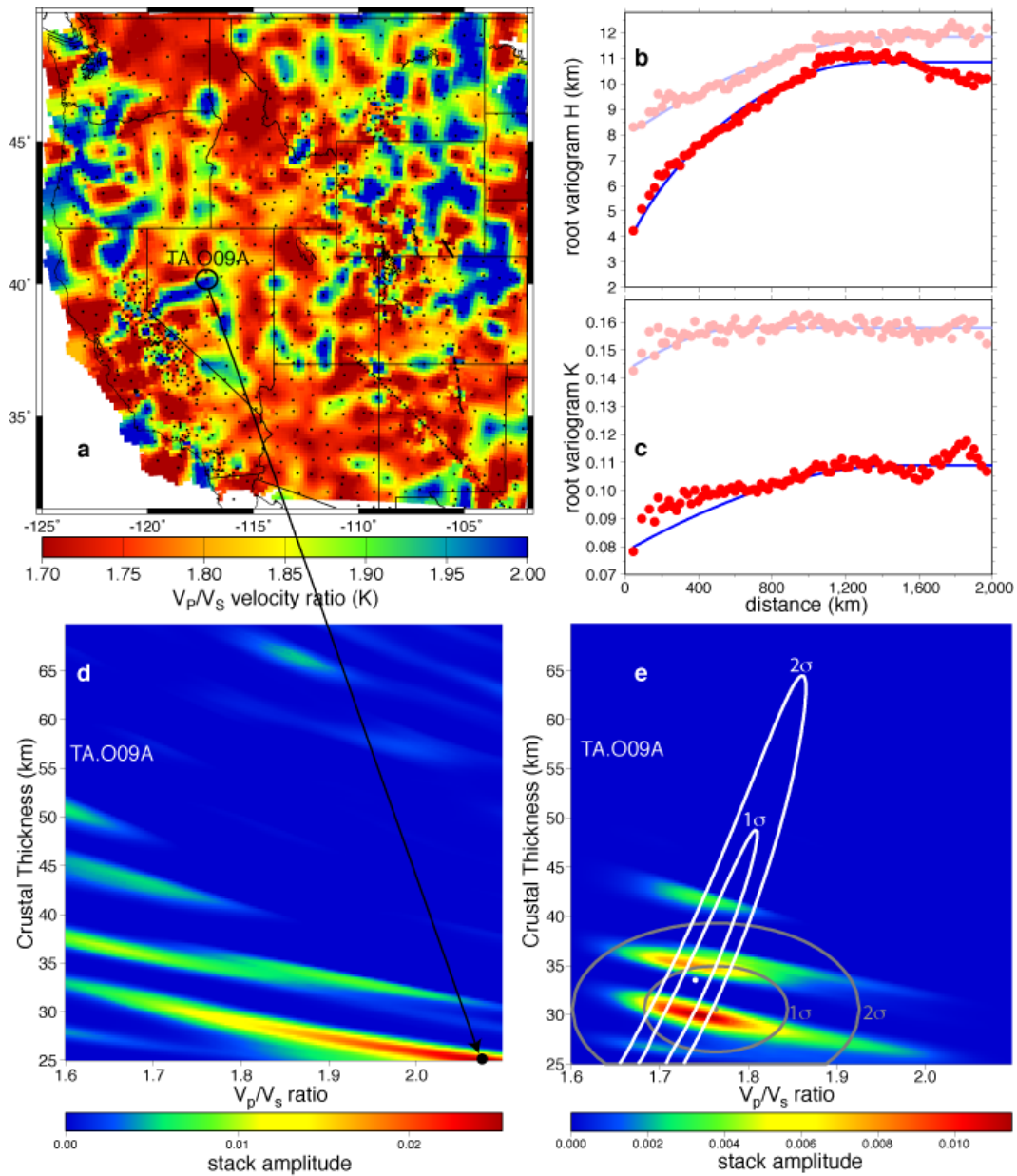


Figure 2. Likelihood filtering of crustal thickness and v_p/v_s . **a**, Raw EARS⁶ estimates of v_p/v_s . **b**, Binned (red circles) and modelled (blue line) root-variograms (root mean squared-difference as a function of distance) of crustal thickness measurements; light colours are raw EARS estimates; full colour saturation, our final model. **c**, Root-variograms of v_p/v_s . **d**, EARS⁶ H - K stack for Transportable Array site O09A ($H = 25$ km; $K = 2.08$). **e**, O09A stack after likelihood filtering ($H = 29.75$; $K = 1.76$). 1-2 σ contours of optimal interpolation (grey) and gravity (white) models used to generate likelihood filters are also shown.

To improve resolution of bulk crustal v_p/v_s , we modified EARS $H-K$ parameter stacks using two likelihood filters: one derived from spatial statistics (using optimal interpolation), and another from gravity modelling of the crustal thickness and v_p/v_s fields (see Methods). Crustal thickness and v_p/v_s parameters trade off unfavourably in both the receiver-function stack (Fig. 2d) and the gravity modelling (Fig. 2e). Combining the information content from the two data sets is advantageous, because the parameter confidence axes are approximately orthogonal, resulting in a ‘cross-hairs’ on the model parameter space (and hence a much improved estimate of v_p/v_s , shown in Fig. 3).

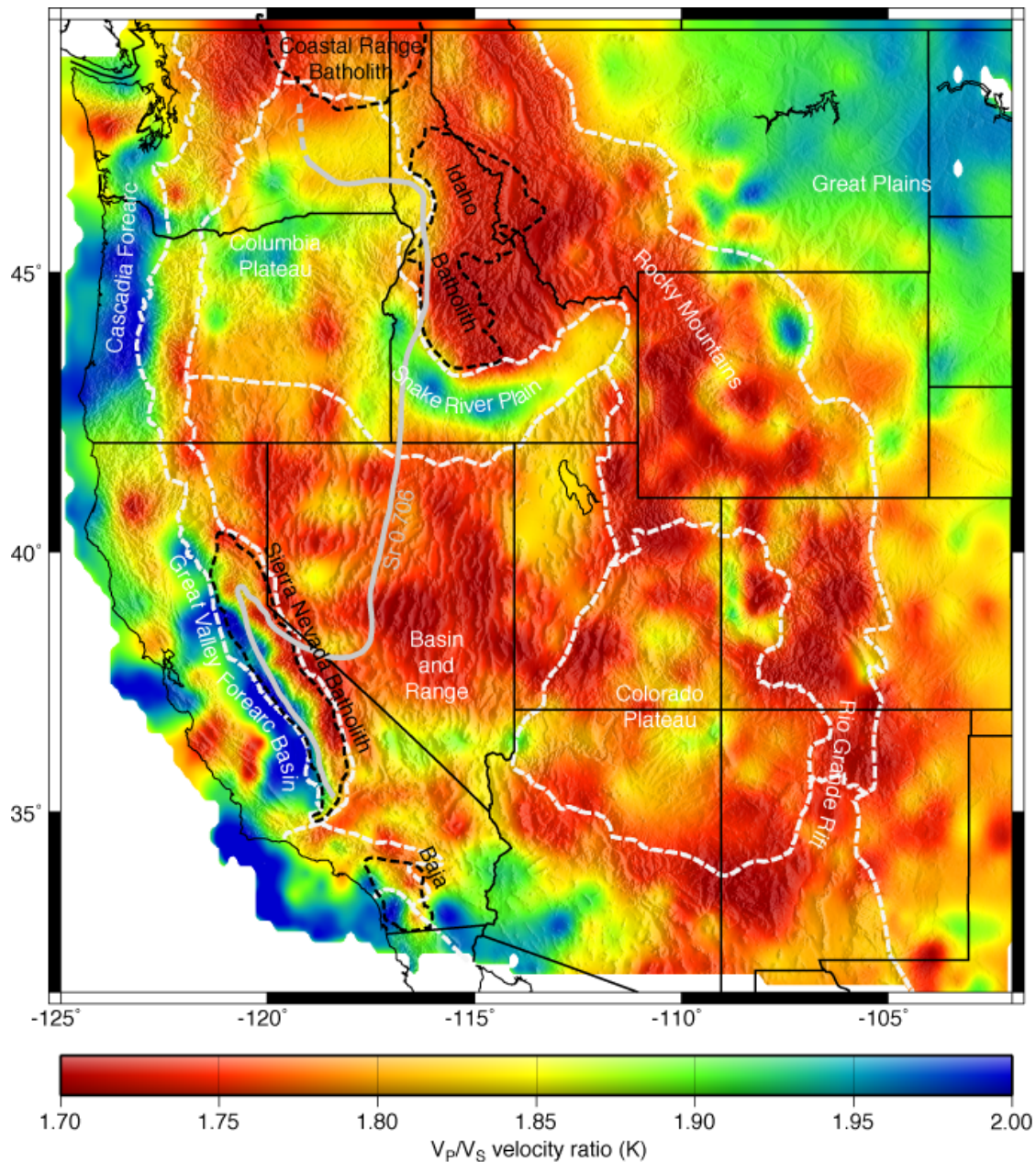


Figure 3. Bulk crustal v_p/v_s of the western United States. Dashed white lines are physiographic province boundaries; dashed black outlines large granitic batholiths; solid grey line is the approximate $^{87}\text{Sr}/^{86}\text{Sr} = 0.706$ isotopic isopleth.

Variations in v_p/v_s have been attributed to both compositional variations and pore fluid pressure effects. High (that is, greater than hydrostatic) pore fluid pressure can significantly raise v_p/v_s , but it would also lower density. In the western United States, composition dominates, as evidenced by the positive sign of the density parameter relating v_p/v_s to observed gravity (grey line in Fig. 1a; see Methods). Figure 3 exhibits high v_p/v_s in several well-studied mafic provinces, including the Snake River plain (where the Yellowstone hotspot has intruded massive quantities of basalt¹³) and oceanic-derived terranes in the Cascadia forearc¹⁴ and the Great Valley forearc basin¹⁵. Crust beneath the Idaho and Coastal Range granitic batholiths has anomalously low v_p/v_s , as it does under eastern parts of the Sierra Nevada and Baja batholiths and the Cascade volcanoes. The $^{87}\text{Sr}/^{86}\text{Sr} = 0.706$ isopleth^{16,17}, a contour of isotopic measurements thought to mark the boundary between young oceanic-derived crust and older, Precambrian continental crust, tracks a sharp boundary between high v_p/v_s to the west and low to the east where the isopleth is well-sampled (California and Idaho).

The variation of v_p/v_s exhibits a remarkable correspondence to the Cenozoic tectonic strain history. The Basin and Range and Rio Grande rifts have relatively low v_p/v_s ratio, particularly along the margins where modern strain rates are highest. The Rocky Mountain provinces (where Laramide thick-skin tectonism was substantial but modern strain-rates are low) also have low v_p/v_s . Deformation-resistant Cordilleran blocks such as the Great Valley, Columbia plateau and Colorado plateau have higher v_p/v_s , as does the stable continental interior, especially in the northern Great Plains.

Perhaps most interesting is the strong inverse correlation observed between v_p/v_s and surface heat flow⁷ (compare Fig. 3 with Fig. 4a). Quantitatively, the correlation coefficient r is -0.56 , significant at more than 26σ confidence, for gravity fields derived from thermal and v_p/v_s models (see Methods and Supplementary Fig. 2). This is surprising, in that the direct effect of temperature on seismic velocities (for example, cyan line in Fig. 1a) would entail high v_p/v_s in warm regions. Thermal conductivity is sensitive to composition¹⁸, but also to temperature, such that granite has 20% greater conductivity than gabbro at the surface, equal conductivity at $\sim 225^\circ\text{C}$ and 30% lower conductivity at 700°C . Hence refractory conduction through the crust, in which three-dimensional heat transfer is favoured in lateral zones of higher conductivity, should yield an opposite-signed relation to that which we observe, and the shallower variations will partially offset the opposite-signed deeper refraction yielding a net-small effect on surface heat flow. Radiogenic heat production is also sensitive to composition, and the relationship predicted between v_p/v_s and heat flow variation has the correct sign, but also would be small relative to measured heat flow variations. Radial v_s anisotropy¹⁹ probably perturbs the signal, and has been observed to be strongest in rifted corridors where advective heat transfer is also greatest. However, the pattern of anisotropy variation is very different to that of v_p/v_s , and the 0–5% measured range of crustal anisotropy roughly maps to the ~ 0.08 1σ uncertainty of the v_p/v_s estimates.

Inverse correlation of v_p/v_s to heat flow makes sense if we consider that advective processes dominate Cordilleran heat flow variations²⁰. Advective processes include lithospheric thinning via rifting²¹, asthenospheric return flow over mantle drips²², and associated processes of magmatism and fluid flux, which are amplified by warming-induced release of water bound in lower-crustal minerals²³. Higher temperatures and water both serve to decrease ductile strength, so puzzling observations like the Wilson cycle, basin inversion and structural reactivation may arise from a geodynamical feedback engendered by variations in crustal silica: ductile strain

initially localizes where quartz concentrations are greatest and the crust is weakest; strain induces lithospheric thinning (in extension) or Rayleigh-Taylor instability (in contraction) which promotes advective heat transfer; the resulting warming hydrates the crust and further weakens the lithosphere, feeding back on the strain localization.

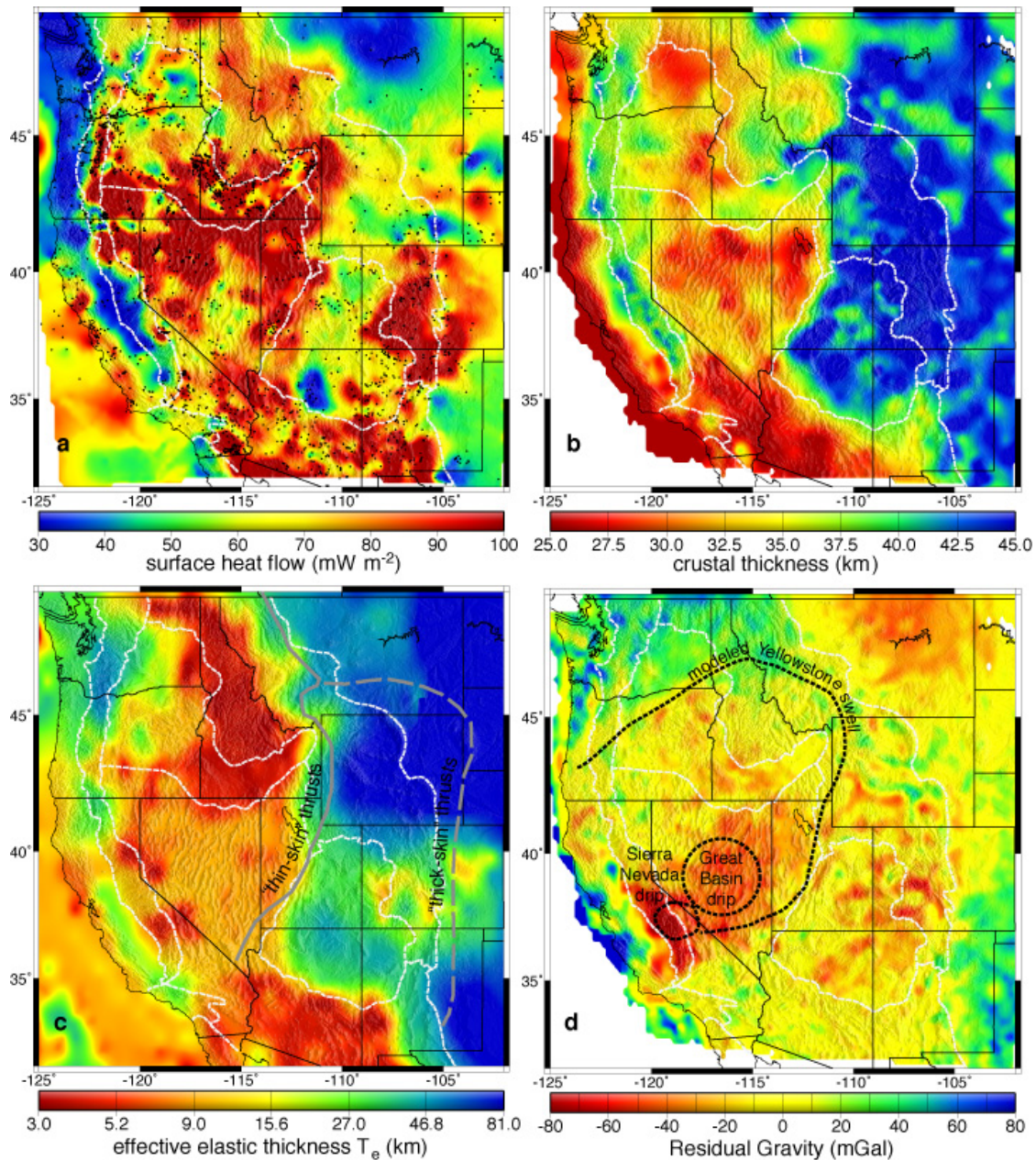


Figure 4. Related fields. Dashed white lines are physiographic province boundaries. **a**, Surface heat flow⁷; black circles are borehole measurement sites. **b**, Crustal thickness. **c**, Effective elastic thickness from coherence analysis of gravity and topography²⁴. Grey lines approximate the eastern limits of Sevier thin-skin contraction (solid) and Laramide foreland thick-skin contraction (dashed). **d**, Residual of the gravity model. Black dashed lines outline potassic volcanism associated with the Sierra Nevada drip²⁶, deeper imaging of the Great Basin drip²⁷, and the 500 m contour of swell elevation modelled for Yellowstone²⁵.

Spatial distributions of deep-derived fluid flux, inferred from surface sampling of $^3\text{He}/^4\text{He}$ and $\delta^{13}\text{C}$ isotopic ratios^{1,11}, lend support to this hypothesis: deep-derived fluid flux is found almost exclusively in regions of low crustal v_p/v_s , opposite to the relationship expected if pore fluid pressure were a significant fraction of the signal⁶. Observations of high CO_2 fluxes¹¹ are consistent with the expectation that CO_2 and water must be present in combination to buffer against resorption of these highly reactive volatiles into crystalline rock²³. These fluids may be an important vector for Cordilleran advective heat transfer, and hence it is conceivable that the relationship of crustal quartz abundance to deformation proposed here would not be possible without the water cycled into the lithosphere during subduction cycles. Of course, not all advective processes begin with surface strain: the Yellowstone-Snake River plain system responded to deep-mantle rather than lithosphere dynamics. But high correlation of lithospheric temperature to crustal composition suggests the feedback mechanism proposed here can be important, and advective heating promoted by deep fluid flux may also lend new insight into the distribution and timing of Cordilleran thermal uplift¹⁰.

Crustal thickness (Fig. 4b) is also inversely correlated with both heat flow ($r = -0.32$) and v_p/v_s ($r = -0.14$). These correlations are highly significant (at $>12\sigma$ and 5σ confidence, respectively), and expected if our proposed dynamical feedback is correct, but coefficients are substantially lower than for v_p/v_s and temperature. A likely reason for weaker correlation of crustal thickness is suggested by the relationship of Cordilleran strain history to lithospheric effective elastic thickness, T_e (Fig. 4c), estimated from an optimized isostatic analysis of gravity and topography²⁴. Modern crustal thickness reflects both orogenic thickening before 30 Myr ago and thinning by subsequent rifting. Values of $T_e > 30$ km imply a contribution of mantle strength²⁵, and whereas extended provinces westward of Sevier-belt thin-skinned contraction exhibit no modern mantle strength, the uppermost mantle under Laramide thick-skinned thrusts remains strong today. Extension has been relatively weak in the Laramide foreland where the mantle is strong. As Laramide thickening focused in regions of more abundant crustal quartz, the net result is thicker crust associated with lower v_p/v_s (whereas in regions of low mantle strength, the opposite is true). There is evidence of latest Quaternary normal faulting throughout the Laramide foreland provinces, however, leaving open the possibility of future weakening. Regardless, the potential for v_p/v_s mapping to help resolve ambiguities in crustal versus mantle contributions to total lithospheric strength is intriguing.

Also of interest is the residual of the gravity model (Fig. 4d). The residual anomalies lend confidence to the inference that unmodelled mass anomalies do not contaminate estimates of the bulk crustal composition, crustal thickness or thermal variation fields. Figure 4d shows recognizable evidence of surficial mass (for example, low density of sedimentary basins) as well as mass variation within the asthenospheric mantle. For example, residual buoyancy centred in the northern Basin and Range is similar to a ‘dynamic elevation’ anomaly previously derived from topography and crustal seismic refraction data, and interpreted as an asymmetric Yellowstone swell²⁵. However, improved resolution by this analysis suggests that return flow over seismically imaged mantle drips^{26,27} may dominate the asthenospheric mass signal. Deep-seated buoyancy anomalies such as these reflect relatively recent changes in temperature towards the base of the thermal boundary layer, and so may prove fruitful locations to look for evidence of the advective transfer processes proposed here.

In initial stages of tectonism (when geotherms are more-or-less uniform), one can reasonably expect strain focusing where crust is silica-rich and hence weak. Laramide thick-skinned thrusting in the middle Rocky Mountains of Wyoming (where modern T_e exceeds 80 km) confirms that crustal strain focusing can occur even in the presence of a thick, strong mantle lithosphere if tectonic forcing is sufficiently robust (for example, during flat-slab subduction). One can also reasonably expect that advective heat transfer processes associated with strain will amplify lithospheric weakness. Comparisons of crustal v_p/v_s to geothermal variations suggest that this dynamical feedback mechanism plays a significant role in defining spatial distributions of tectonic strain and uplift. Examining these in the context of total lithospheric strength may improve our understanding of the roles played by the crust and mantle. EarthScope will afford an important test of the hypothesis as it moves further east and traverses the Appalachian orogeny, where Wilson first postulated cyclical repetition of tectonic events³.

METHODS SUMMARY

The analysis developed for this study introduces several innovations to the combination of complementary geophysical data. The primary data set consisted of EARS⁶ $H-K$ parameter stacks of seismic receiver-function amplitudes. Structures at crustal depths (that is, less than 50 km) are spatially aliased by near-vertical arrivals to EarthScope's transportable array, which samples at a nominal 70 km spacing. Uncertainties inherent in a lack of redundant sampling of the crust were mitigated using spatial statistics, by deriving likelihood filters at each site from optimal interpolations (OI) of the crustal thickness and v_p/v_s estimates at neighbouring sites. A second likelihood filter was derived by modelling the Bouguer gravity field predicted by estimates at surrounding sites, allowing crustal thickness and v_p/v_s to vary at the site of interest, and comparing to measured gravity. The combination of these filters emphasizes receiver-function stack amplitude maxima within the model-space of high likelihood rather than forcing a model parameterization preferred by the OI or gravity models. Gravity contains signals from other mass fields besides crustal thickness and crustal composition, however, and within the study region the largest is mass related to geotherm variations, or thermal mass. Thermal mass was modelled independently from geotherms estimated using surface heat flow measurements⁷ and surface radiogenic element concentrations derived from airborne γ -ray spectroscopy measurements^{28,29}. The combination of these was used to derive a model of crustal radiogenic heat production before calculation of the thermal structure. The geotherm estimates implicitly include an advective contribution to heat transfer from extensional strain²⁵; strain rates required to maintain the measured heat flow are generally two to five times larger than geodetically observed rates, suggesting a significant role for magmatic and hydrothermal processes in Cordilleran advective heat transfer. Additional methodological details are provided in Online Methods.

Received 7 October 2010; accepted 10 February 2011; doi:10.1038/nature09912.

1. Williams, M. L. et al. Unlocking the secrets of the North American continent: an EarthScope science plan for 2010–2020. (<http://www.earthscope.org/ESSP>) (2010).
2. Bürgmann, R. & Dresen, G. Rheology of the lower crust and upper mantle: evidence from rock mechanics, geodesy and field observations. *Annu. Rev. Earth Planet. Sci.* **36**, 531–567 (2008).
3. Wilson, J. T. Did the Atlantic close and then re-open? *Nature* **211**, 676–681 (1966).

4. Ziegler, P. A. et al. Dynamics of intra-plate compressional deformation: the Alpine foreland and other examples. *Tectonophysics* **252**, 7–59 (1995).
5. Sykes, L. R. Intraplate seismicity, reactivation of pre-existing zones of weakness, alkaline magmatism, and other tectonism postdating continental fragmentation. *Rev. Geophys.* **16**, 621–688 (1978).
6. Crotwell, H. P. & Owens, T. J. Automated receiver function processing. *Seismol. Res. Lett.* **76**, 702–709 (2005); data available at www.iris.washington.edu/ears.
7. Blackwell, D. & Richards, M. *Geothermal Map of North America, 2004* (scale 1:6,500,000, AAPG Item 423, 2004); data available at <http://smu.edu/geothermal>.
8. Christensen, N. I. Poisson's ratio and crustal seismology. *J. Geophys. Res.* **101**, 3139–3156 (1996).
9. Kono, Y., Miyake, A., Ishikawa, M. & Arima, M. Temperature derivatives of elastic wave velocities in plagioclase (An_{51±1}) above and below the order-disorder transition temperature. *Am. Mineral.* **93**, 558–564 (2008).
10. Roy, M., Jordan, T. H. & Pederson, J. Colorado Plateau magmatism and uplift by warming of heterogeneous lithosphere. *Nature* **459**, 978–982 (2009).
11. Crossey, L. J. et al. Degassing of mantle-derived CO₂ and He from springs in the southern Colorado Plateau region: neotectonic connections and implications for groundwater systems. *Geol. Soc. Am. Bull.* **121**, 1034–1053 (2009).
12. Zhu, L. & Kanamori, H. Moho depth variation in Southern California from teleseismic receiver functions. *J. Geophys. Res.* **105**, 2969–2980 (2000).
13. Smith, R. B. & Braile, L. W. The Yellowstone hotspot. *J. Volcanol. Geotherm. Res.* **61**, 121–187 (1994).
14. Trehu, A. M. et al. Crustal architecture of the Cascadia fore-arc. *Science* **266**, 237–243 (1994).
15. Godfrey, N. J. & Klemperer, S. L. Ophiolitic basement to a forearc basin and implications for continental growth: the Coast Range Great Valley ophiolite, California. *Tectonics* **17**, 558–570 (1998).
16. Kistler, R. W. & Ross, D. C. A strontium isotopic study of plutons and associated rocks of the southern Sierra Nevada and vicinity, California. *US Geol. Surv. Bull.* **1920**, 20pp (1990).
17. Fleck, R. J. & Criss, R. E. Location, age, and tectonic significance of the Western Idaho Suture Zone (WISZ). *US Geol. Surv. Open File Rep.* **2004-1039**, 48pp (2004).
18. Kukkonen, I. T., Jokinen, J. & Seipold, U. Temperature and pressure dependencies of thermal transport properties of rocks: implications for uncertainties in thermal lithosphere models and new laboratory measurements of high-grade rocks in the central Fennoscandian Shield. *Surv. Geophys.* **30**, 33–59 (1999).
19. Moschetti, M. P., Ritzwoller, M. H., Lin, F. & Lang, Y. Seismic evidence for widespread western-US deep-crustal deformation caused by extension. *Nature* **464**, 885–889 (2010).

20. Sass, J. H. et al. Thermal regime of the southern Basin and Range Province 1. Heat-flow data from Arizona and the Mojave Desert of California and Nevada. *J. Geophys. Res.* **99**, 22093–22119 (1994).
21. McKenzie, D. Some remarks on development of sedimentary basins. *Earth Planet. Sci. Lett.* **40**, 25–32 (1978).
22. Molnar, P., England, P. & Martinod, J. Mantle dynamics, uplift of the Tibetan Plateau, and the Indian monsoon. *Rev. Geophys.* **31**, 357–396 (1993).
23. Yardley, B. W. D. The role of water in the evolution of the continental crust. *J. Geol. Soc. Lond.* **166**, 585–600 (2009).
24. Pérez-Gussinyé, M. et al. Effective elastic thickness of Africa and its relationship to other proxies for lithospheric structure and surface tectonics. *Earth Planet. Sci. Lett.* **287**, 152–167 (2009).
25. Lowry, A. R., Ribe, N. M. & Smith, R. B. Dynamic elevation of the Cordillera, western United States. *J. Geophys. Res.* **105**, 23371–23390 (2000).
26. Zandt, G. et al. Active foundering of a continental arc root beneath the southern Sierra Nevada in California. *Nature* **431**, 41–46 (2004).
27. West, J. D., Fouch, M. J., Roth, J. B. & Elkins-Tanton, L. T. Vertical mantle flow associated with a lithospheric drip beneath the Great Basin. *Nature Geosci.* **2**, 439–444 (2009).
28. Duval, J. S., Carson, J. M., Holman, P. B. & Darnley, A. G. Terrestrial radioactivity and gamma-ray exposure in the United States and Canada. *US Geol. Surv. Open File Rep.* **2005-1413**, (2005).
29. Kucks, R. P. Terrestrial radioactivity and gamma-ray exposure in the United States and Canada: Gridded geographic images. *US Geol. Surv. Open File Rep.* **2005-1413**, (2005); available at <http://pubs.usgs.gov/of/2005/1413>.

Supplementary Information is linked to the online version of the paper at www.nature.com/nature.

Acknowledgements We thank K. Dueker, G. Pavlis, T. Ravat, J. Shervais and D. Schutt for discussions, and A. Braathen and R. Bürgmann for comments. We are grateful to P. Crotwell, T. Owens and members of IRIS for their efforts on the EARS database, and to Crotwell and B. Kucks for help with data acquisition. The work of A.R.L. on this project was supported by National Science Foundation grants EAR-0454541 (EarthScope Science: Rio Grande Rift) and EAR-0955909 (Geophysics/EarthScope CAREER: Deformation Processes), and by a Utah State University New Faculty Research Grant.

Author Contributions A.R.L. developed and implemented the joint receiver function/gravity/heatflow inversion for crustal thickness and v_p/v_s . M.P.-G. developed and implemented the inversion for effective elastic thickness. The manuscript was written by A.R.L. with contributions from M.P.-G.

Author Information Reprints and permissions information is available at www.nature.com/reprints. The authors declare no competing financial interests. Readers are welcome to comment on the online version of this article at www.nature.com/nature. Correspondence and requests for materials should be addressed to A.R.L. (Tony.Lowry@usu.edu).

ONLINE METHODS

The joint seismic receiver function/gravity/heat flow inversion for estimating crustal thickness (H) and v_p/v_s (K) iteratively applies several data modelling and inversion procedures, summarized as a sequence of the following steps: (1) Calculate variograms of the H and K estimates. (2) Using observed Bouguer gravity data, linearly invert for optimal density parameters associated with the H and K fields plus a thermal boundary layer model derived from surface heat flow data. (3) Calculate a likelihood filter of the (H , K) parameter space at site S_i using optimal interpolation (OI) with variograms estimated in step 1. (4) Calculate a second likelihood filter at site S_i from localized gravity modelling using density parameters estimated in step 2. (5) Multiply the likelihood filters by the EARS⁶ H - K stack at site S_i , and set (H_i , K_i) to the filtered stack maximum. (6) Set $i = i + 1$ and continue from step 1.

Step 1: variogram estimation.

We use raw EARS⁶ H - K parameter amplitude stacks as our receiver-function observable. Amplitude maxima from the raw stacks are assumed as the starting model of crustal thickness H and v_p/v_s ratio K . Measurement pairs are binned according to the distance between, and the variograms (that is, expected value of the squared difference as a function of distance between measurements) are estimated. Variograms of the initial (EARS⁶) and final models of H (Fig. 4b) and K (Fig. 3) are shown in Fig. 2b and c respectively. Optimal interpolation (OI, also referred to as ‘kriging’) uses the data variograms to interpolate data based on distance to, and estimates at, nearby measurements³⁰.

Step 2: estimation of density parameters.

Modelling the gravity likelihood filter in step 4 requires an estimate of the three density parameters that relate H , K and thermal variations to gravity. Laboratory measurements and geophysical models of the Moho density contrast, $\Delta\rho_{\text{Moho}}$, the partial derivative of density with respect to v_p/v_s ratio, $\partial\rho/\partial K$, and the coefficient of thermal expansion, α_v , depend on rock composition and other factors that vary spatially, so the *in situ* values are a priori unknown. Consequently we chose to estimate a representative regional average of these parameters directly from the relationship of the fields to observed gravity within the approximate current footprint of the EarthScope Transportable Array.

We first calculate Bouguer gravity fields per unit density, B_H^1 , B_K^1 and B_T^1 , by neglecting the density parameters $\Delta\rho_{\text{Moho}}$, $\partial\rho/\partial K$ and α_v . We reference all estimates of crustal thickness H to a datum (that is, subtract the site elevations) and then optimally interpolate H and K to a 16-km mesh grid covering the region from 32–49° N latitude, 102–125° E longitude. Means \bar{H} and \bar{K} are then removed, and the fields are mirrored and Fourier-transformed to frequency domain amplitudes $\tilde{H} = F\{H - \bar{H}\}$ and $\tilde{K} = F\{K - \bar{K}\}$, where $F\{\bullet\}$ denotes the Fourier transform operator. We calculate Fourier amplitudes of the Bouguer per unit Moho density contrast, \tilde{B}_H^1 , associated with the H field via:

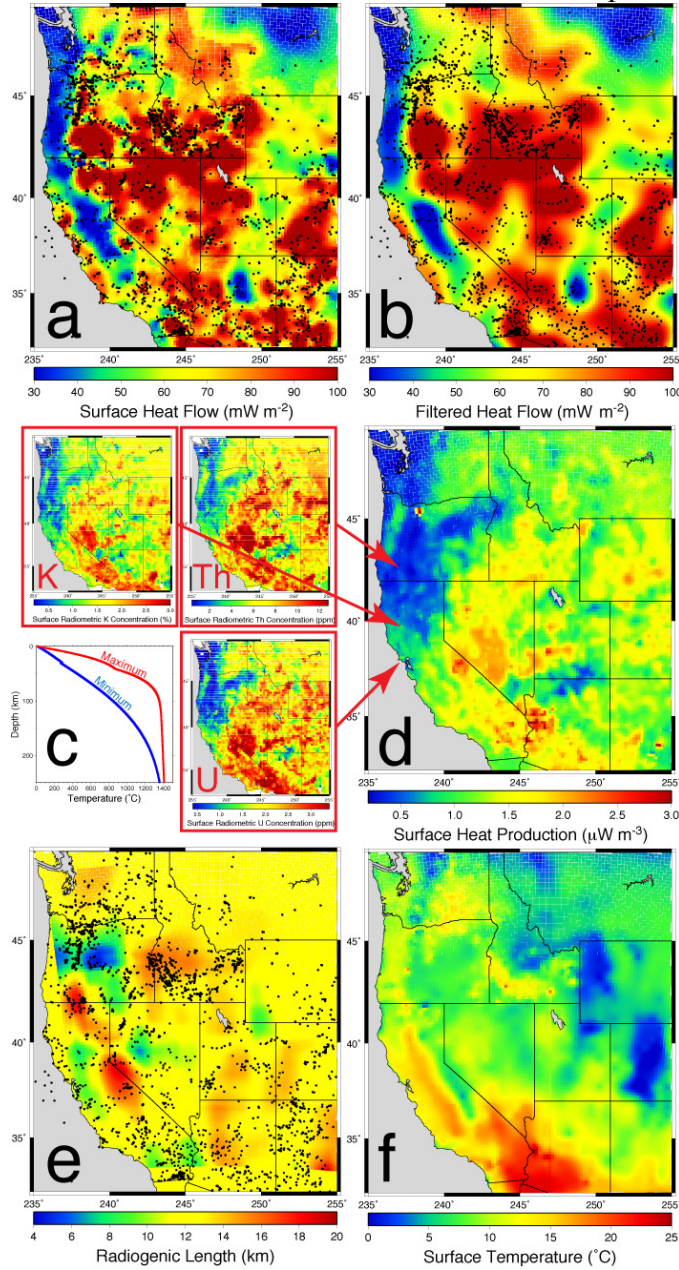
$$\tilde{B}_H^1 = 2\pi G \tilde{H} \exp(-k\bar{H}) \quad (1)$$

where G is the universal gravitational constant and k is modulus of the two-dimensional wavenumber associated with each Fourier amplitude. The Bouguer per unit density amplitudes,

\tilde{B}_K^1 , associated with K are calculated via:

$$\tilde{B}_K^1 = 2\pi G \left[\frac{1 - \exp(-k\bar{H})}{k} \tilde{K} - \tilde{M} \exp(-k\bar{H}) \right] \quad (2)$$

in which $\tilde{M} = F\{(H-\bar{H})(K-\bar{K})\}$ is a correction factor for variable crustal thickness.



Supplementary Figure S1 | Data sets and processing steps used in thermal modeling. **a**,

Raw surface heat flow⁷ q_s . Black circles are measurement locations. **b**, Heat flow after filtering to remove shallow sources and sinks. **c**, Red boxes hold concentrations of radioactive elements measured with airborne γ -ray spectroscopy^{29,30}; inset lower-left shows minimum and maximum geotherm estimates modeled here. **d**, Surface heat production A_0 combines K, Th and U contributions from (c). **e**, Length parameter of decreased heat production, l_{rad} . **f**, Surface mean temperature³¹ T_s .

Because thermal variations contribute significantly to the total gravity used here to invert for crustal thickness and composition, a correction for estimated thermal mass is included in the model. The model of thermal gravity uses a geotherm inverted from data that include surface heat flow measurements⁷, q_s , airborne γ -ray spectroscopy measurements of surface radiogenic element concentrations^{28,29}, and mean annual surface temperature data³¹. Supplementary Fig. 1a depicts the OI of heat flow measurements⁷. These were extrapolated to depth using one-dimensional heat-

transfer relations that assume steady-state advection by extensional strain²⁵, and a thermal conductivity, κ , with temperature-dependent parameterization³² that averages crustal and mantle rock types¹⁶. We assume mantle potential temperature $T_r = 1,320$ °C, and an adiabat is derived for pressure/temperature-dependent values of mantle coefficient of thermal expansion and specific heat capacity³³. The airborne γ -ray spectroscopy measurements^{28,29} of U, Th and K radiogenic element concentrations (Supplementary Fig. 1c) are converted to surface heat production, A_0 , (Supplementary Fig. 1d) via³⁴:

$$A_0 = \rho(3.58 \times 10^{-5} C_K + 2.69 \times 10^{-5} C_{Th} + 9.71 \times 10^{-5} C_U) \quad (3)$$

in which C_X are concentrations in parts per billion. Weighted least squares regression of the relationship between q_s and A_0 within 500 km windows yields estimates of a length-scale for an exponential depth decay, l_{rad} , that are physically reasonable (Supplementary Fig. 1e); a posteriori (that is, misfit-scaled) parameter uncertainties of radiogenic length estimates are typically 10–30%. In the absence of better constraint, this approach adequately represents the spatial distribution of heat producing elements.

After subtracting the portion arising from shallow heat production, heat flow is filtered³⁵ to remove effects of sources and sinks shallower than 30 km (Supplementary Fig. 1b). This removes most (though not all) advective effects of near-surface hydrology and heat flow measurement noise associated with three-dimensional conductivity variations and topographic effects. Temperature is estimated as²⁵:

$$T(z) = T_s + \frac{A_0 l_{\text{rad}}^2}{\kappa} \left[1 - \exp\left(-\frac{z}{l_{\text{rad}}}\right) \right] + \left(T_r - \frac{A_0 l_{\text{rad}}^2}{\kappa} - T_s \right) \text{erf}\left(\frac{z}{l_{\text{con}}}\right) \quad (4)$$

where

$$l_{\text{con}} = \frac{2 \left[\kappa (T_r - T_s) - A_0 l_{\text{rad}}^2 \right]}{\sqrt{\pi} (q_s - A_0 l_{\text{rad}})} \quad (5)$$

and the minimum and maximum estimates of geotherms from the map region are shown in Supplementary Fig. 1c inset. (Note the actual relations used are complicated slightly, relative to equations (4) and (5), by the temperature-dependence of κ and a solution for two relations, one each for the crust and mantle, with stipulation that temperature and heat flux for both are identical at the Moho).

Supplementary Fig. 1f shows the surface temperature, T_s , adapted from climate models of mean annual temperature³¹. An advective contribution from extensional strain (needed to accommodate advective heat transfer) is implicit rather than explicit in these relations. Map-view thermal fields, T_z , are averaged over 1-km depth ranges for $z = 1, \dots, 200$ km, means are removed, and the data are mirrored and transformed as $\tilde{T}_z = F \{T_z - \bar{T}_z\}$. Then amplitudes of the thermal gravity field per unit density variation, B_T^1 , are calculated via:

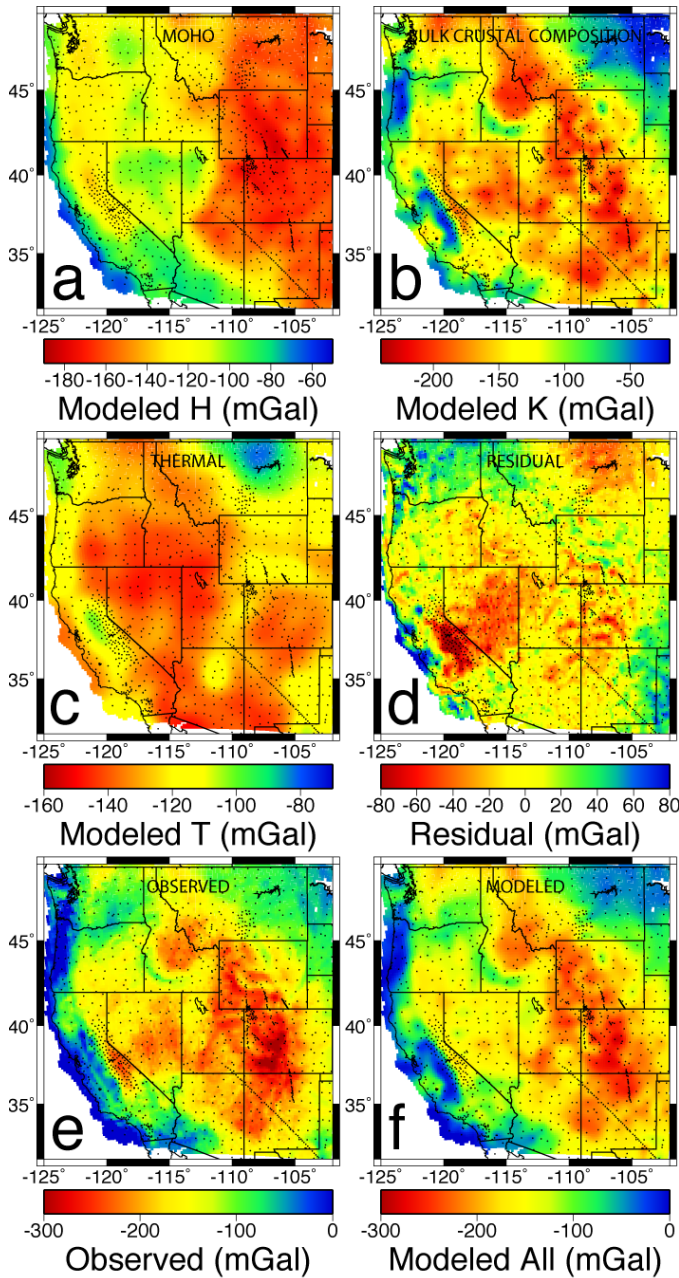
$$\tilde{B}_T^1 = 2,000\pi G \sum_{z=1}^{200} \bar{\rho}_z \tilde{T}_z \exp(-kz) \quad (6)$$

Here $\bar{\rho}_z$ is an expected value for density at a given depth, based on the mean temperature and a continental mean compositional profile with depth³⁶. Note the multiplication by factor-of-1,000 arises from the 1-km discretisation of the geotherm.

We now have amplitudes for three different gravity fields, B_H^1 , B_K^1 and B_T^1 , that are independent of density parameters. To estimate those density parameters, we inverse transform the amplitudes to the spatial domain, strip mirrored portions and then invert the highly over-determined system of linear equations:

$$\bar{B}_H^1 \Delta \rho_{\text{Moho}} + \bar{B}_K^1 \frac{\partial \rho}{\partial K} + \bar{B}_T^1 \alpha_v + \bar{1}s = \bar{B}_{\text{obs}} \quad (7)$$

for the unknown parameters $\Delta\rho_{\text{Moho}}$, $\partial\rho/\partial K$, α_v , and a static offset s . Here, the arrow denotes a $\sim 15,000 \times 1$ vector.

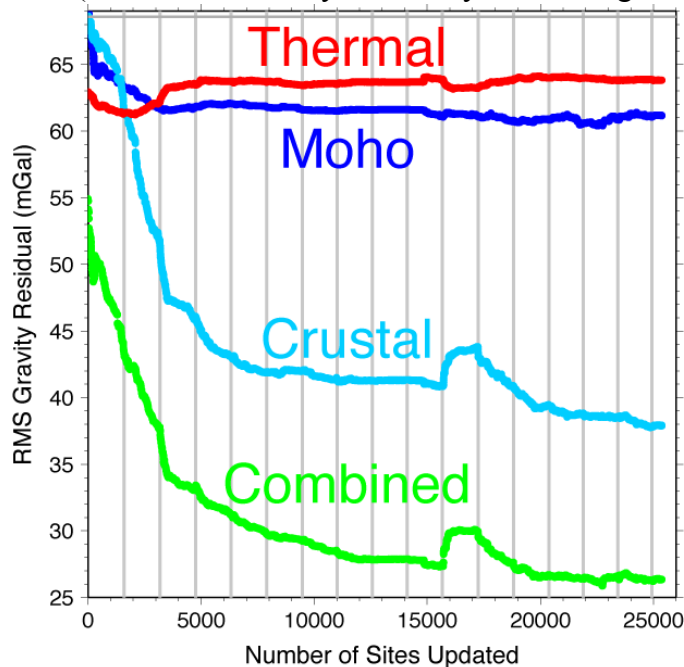


Supplementary Figure S2 | Modeled and observed Bouguer gravity fields. **a**, Final model of Moho gravity ($B_H^1 \Delta\rho_{\text{Moho}}$). Black circles denote seismic sites. **b**, Final model of crustal gravity ($B_K^1 \partial\rho/\partial K$). **c**, Thermal gravity ($B_T^1 \alpha_v$). **d**, Residual (observed minus sum of models). **e**, Observed Bouguer gravity. **f**, Model summing Figs. S2a-c.

Supplementary Fig. 2 depicts each of the individual components of the final regional model of the gravity field (Supplementary Fig. 2a–c), the observed-minus-modelled residual (Supplementary Fig. 2d; see also Fig. 4d), the observed gravity field (Supplementary Fig. 2e), and the total modelled gravity field summing contributions from the Moho, crustal density variations and thermal density variations (Supplementary Fig. 2f). It is worth noting that the mass fields derived from this gravity modelling can be used for geodynamical investigations of stress, strain and isostatic loading, and in fact estimation of these mass fields was the original objective of this investigation. Supplementary Fig. 3 depicts evolution of the r.m.s. gravity residual for the summed model, and for separate components of the model, over $\sim 25,000$ site updates (roughly 16 iterations over all seismic sites within the map space). Residual of the summed model drops from 55 mGal for the starting model, using raw EARS estimates of H and K , to 26 mGal for the final model. By

comparison, the root-variance of observed gravity is 68 mGal. (Note that the deviation beginning around 15,000 site updates resulted after introduction of new H – K stacks from the IRIS database⁶. The iterative inversion results shown here required about six months of computation on a quad-core workstation, during which time the EarthScope Transportable Array continued to collect new earthquake data and add new sites). Taken separately, the raw EARS data contribute virtually no reduction of variance to the starting model. Hence, the thermal model dominates total reduction of variance when the raw EARS estimates are used, that is, at iteration 0 in Supplementary Fig. 3. The temperature model does not change during the inversion run (although the thermal density parameter, α_v , does), and contributions from the Moho and crustal

density models overtake the thermal mass contribution by the end of the second iteration over all sites (with crustal density eventually dominating the overall reduction of gravity variance).



Supplementary Figure S3 | Evolution of the gravity model. RMS residual for models of thermal gravity ($B_T^1 \alpha_v$) are shown as red circles, Moho gravity ($B_H^1 \Delta \rho_{Moho}$) are blue, bulk crustal gravity ($B_K^1 \partial \rho / \partial K$) are cyan, and the combined model of Bouguer gravity (summing the three components) is green. Horizontal grey bar is RMS of the observed gravity field; vertical bars demark iterations over the entire map space.

The final density parameter estimates are $0.81 \times 10^{-5} \text{ } ^\circ\text{C}^{-1}$ for the coefficient of thermal expansion α_v , 115 kg m^{-3} for $\Delta \rho_{Moho}$, and 460 kg m^{-3} for $\partial \rho / \partial K$. These values differ slightly from expectations based on laboratory experiments and other geophysical studies. Laboratory data on pressure- and temperature-dependence of the thermal

expansion coefficient for rocks within the thermal boundary layer predict values in the range $(0.5\text{--}3.5) \times 10^{-5} \text{ } ^\circ\text{C}^{-1}$. The low estimate derived here is consistent with predictions for granite³⁷, but the upper mantle (where α_v should be $(2.5\text{--}3.5) \times 10^{-5}$; ref. 38) dominates the thermal mass integral (Supplementary Fig. 1c inset). Recent studies suggest the effective thermal expansivity of a viscoelastic fluid mantle will be 15–30% less than laboratory mineral physics measurements of the volumetric coefficient of thermal expansion^{39,40}, but the ~70% lower value estimated here is more likely to reflect a poor geotherm model. Surface heat flow measurements are sparse and notoriously noisy, and non-steady-state contributions to lithospheric heat transfer (for example, under the Sierra Nevada⁴¹ and the Colorado plateau²³) cannot be modelled accurately from surface data alone, so the thermal model used here is likely to represent mantle temperature variations poorly. One implication of this is that the true correlation coefficient of geothermal variations and crustal composition may be even higher than we have estimated.

The density contrast for continental Moho inferred from normal mode seismic analysis is 480 kg m^{-3} (ref. 42), but laboratory measurements indicate it can range from about -200 to 600 kg m^{-3} and globally averages $\sim 230 \text{ kg m}^{-3}$ (ref. 36). Our final crustal thickness estimates (Fig. 4b) match fairly well the independent estimates from more sparsely sampled crustal seismic refraction studies (for example, compiled in ref. 25) and from inversion of Rayleigh phase velocity data (D. Schutt, personal communication). The regression slope of the latter independent estimate with ours is 1.001 with a correlation coefficient of 0.72, so the density contrast estimate is unlikely to be significantly in error. Much of the thicker crust in western portions of the region of our inversion is underlain by dense cumulates and/or eclogites, for example, under the Sierra Nevada²⁶, Cascade Range and the Snake River plain⁴³; other regions of thick crust (such as the Wyoming province⁴⁴) exhibit anomalously high lower crustal velocity. These would imply a lower-than-average Moho density contrast. Laboratory measurements suggest the partial derivative of density with respect to v_p/v_s deriving from compositional variations should be

around $1,500 \text{ kg m}^{-3}$ (Fig. 1a), although this will vary significantly depending on actual abundances of various compositions, and the direct effect of temperature on v_p/v_s effectively would lower the observational slope.

Step 3: OI likelihood filter.

OI yields both an expected value and an estimate of uncertainty, and we use it in this application both for interpolation of various measurement fields to arbitrary locations and for estimation of likelihood functions applied to H - K stacks. The OI likelihood filter at a seismic site S_i chosen for update is estimated by interpolating H and K estimates from the 150 nearest sites to the location of site S_i . The expected values (H_i^{OI} , K_i^{OI}) and 1σ estimates of uncertainty (σ_H , σ_K) are used to determine OI confidence interval C_{OI} at all stack amplitude realizations (H_a , K_a) present in the EARS stack via:

$$C_{\text{OI}}^2(H_a, K_a) = \left(\frac{H_a - H_i^{\text{OI}}}{\sigma_H} \right)^2 + \left(\frac{K_a - K_i^{\text{OI}}}{\sigma_K} \right)^2 \quad (8)$$

Then, assuming H and K are Gaussian processes, C_{OI} will be χ^2 -distributed and the likelihood corresponding to that confidence interval is given by⁴⁵:

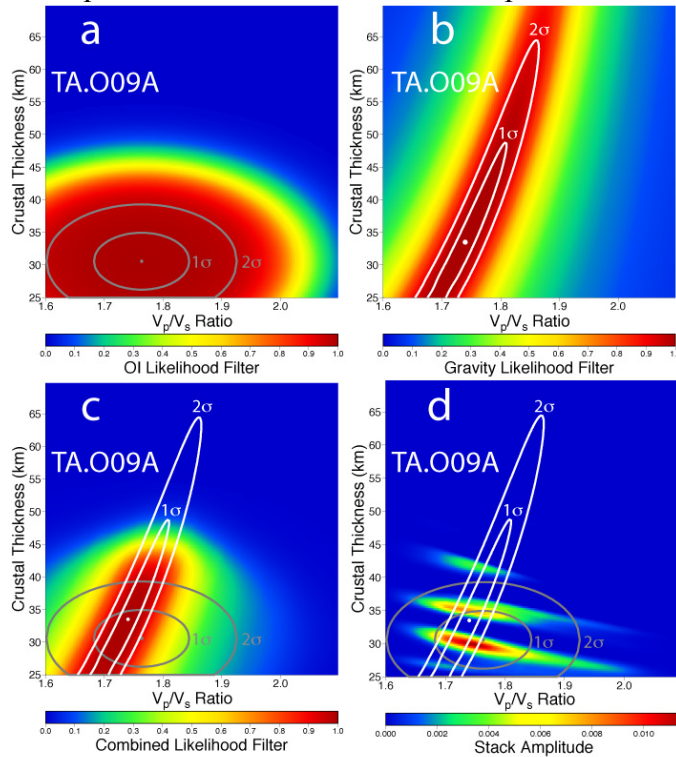
$$L = \frac{1}{\sqrt{1 + \frac{M}{N-M} F_{\alpha}^{-1}(M, N-M)}} \quad (9)$$

Here the degrees of freedom are those of the H - K stack: M , the number of model parameters, is 2 (being H and K); the number of observations $N = 4n$ where n is the number of earthquakes used in the stack and 4 represents the number of seismic phases sampled (Ps, PpSs,

PsPs and PpPs), F^{-1} is the inverse of the F -cumulative distribution function, and α represents the probability:

$$\alpha = \exp\left(-\frac{C_{\text{OI}}^2}{2}\right) \quad (10)$$

An example OI likelihood filter $L(H, K)$ at Nevada site TA.O09A is shown in Supplementary Fig. 4a.



Supplementary Figure S4 | Example likelihood filters for site TA.O09A in central Nevada. **a**, Likelihood filter from optimal interpolation (OI); grey contours are confidence intervals. **b**, Filter from gravity modeling; white contours are confidence intervals. **c**, Combined filter using gravity and OI. **d**, Filtered amplitude stack (identical to Fig. 2e).

Step 4: gravity likelihood filter.

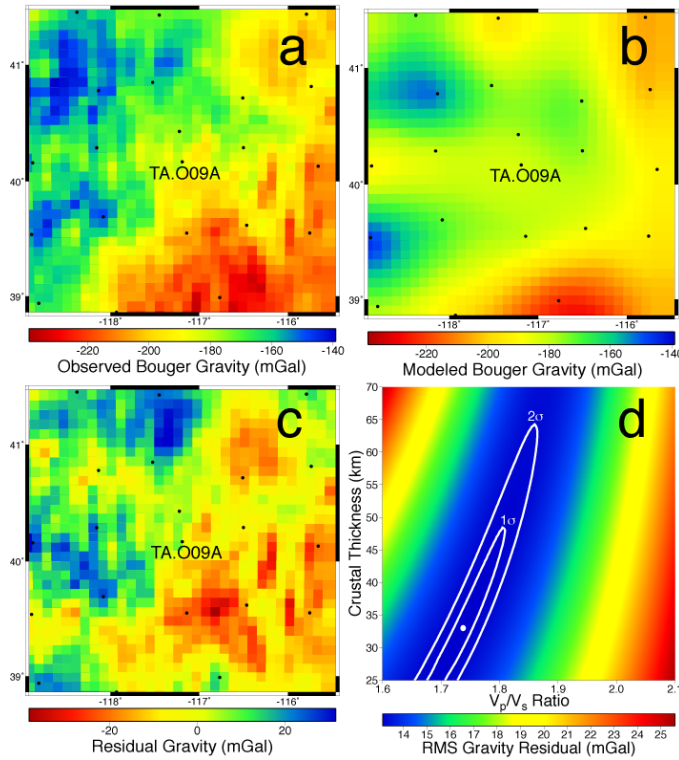
A second likelihood filter is derived from gravity modelling within a relatively small

window near the seismic site. For each possible permutation of (H_a, K_a) represented in the EARS amplitude stack, we temporarily set (H_i, K_i) at the update site S_i equal to (H_a, K_a) and hold fixed the crustal thickness and v_p/v_s ratio at surrounding sites. We reference crustal thickness H to a datum (that is, subtract the site elevation) and then optimally interpolate H and K to a 9-km mesh, 288-km aperture grid centred at site S_i . The gravity modelling is analogous to that used to estimate density parameters in step 2, except that now we model Bouguer gravity (that is, using the estimated density parameters) rather than gravity per unit density. Means \bar{H} and \bar{K} are removed, the fields are mirrored and Fourier-transformed to frequency domain amplitudes $\tilde{H} = F\{H - \bar{H}\}$ and $\tilde{K} = F\{K - \bar{K}\}$, and we calculate amplitudes of the Bouguer gravity fields \tilde{B}_H associated with the H field via:

$$\tilde{B}_H = 2\pi G \Delta\rho_{Moho} \tilde{H} \exp(-k\bar{H}) \quad (11)$$

\tilde{B}_K associated with K via:

$$\tilde{B}_K = 2\pi G \frac{\partial\rho}{\partial K} \left[\frac{1 - \exp(-k\bar{H})}{k} \tilde{K} - \tilde{M} \exp(-k\bar{H}) \right] \quad (12)$$



and \tilde{B}_T for the thermal model as:

$$\tilde{B}_T = 2,000\pi G \alpha_v \sum_{z=1}^{200} \bar{\rho}_z \tilde{T}_z \exp(-kz) \quad (13)$$

Supplementary Figure S5 | Site-specific gravity modeling example for central Nevada site TA.009A. **a**, Observed Bouguer gravity; small black circles represent other nearby seismic sites with EARS stacks. **b**, Best-fit modeled gravity ($H_a = 33$ km; $K_a = 1.74$). **c**, Observed minus modeled residual. **d**, RMS misfit as a function of assumed (H_a, K_a) at site $S_i = TA.009A$; white contours are confidence intervals.

We inverse transform gravity fields to the spatial domain, strip mirrored portions and calculate a modelled gravity field B_{Mod} by summing B_H , B_K and B_T . Example observed and modelled gravity for the TA.009A site is shown in Supplementary Fig. 5a and b, respectively. We then subtract the mean difference

between modelled and observed gravity, and calculate the L_2 -norm of the residual difference (Supplementary Fig. 5c). The r.m.s. misfit, R , as a function of assumed (H_a, K_a) at the site (Supplementary Fig. 5d) can be used to derive confidence intervals on the gravity model via the likelihood ratio method⁴⁵, in which the confidence region with probability α of containing the correct solution corresponds to the model space for which

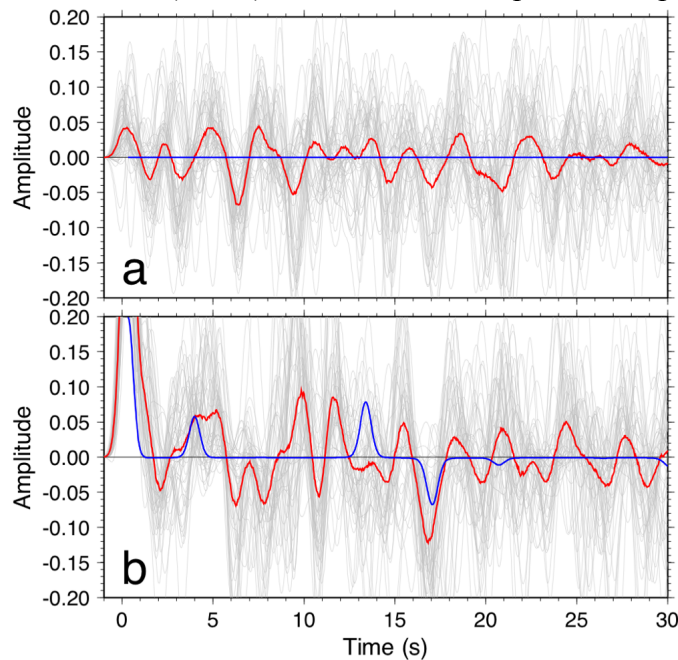
$$R^2 \leq R_{\min}^2 \left[1 + \frac{M}{N_g - M} F_{\alpha}^{-1}(M, N_g - M) \right] \quad (14)$$

where N_g is the number of gravity observations and R_{\min} is the global minimum gravity residual. We map R^2 to given probability α and then use α as a function of H - K to calculate a likelihood filter for the stack amplitude, using equation (9). This effectively transforms the misfit function from the gravity modelling to the degrees-of-freedom inherent to the receiver function stack. An example likelihood filter derived from gravity modelling at site TA.O09A is shown in Supplementary Fig. 4b.

Step 5: updating the H - K estimate at a site.

Both the OI and gravity likelihood filters (Supplementary Fig. 4c) are multiplied by the raw EARS receiver function amplitude stack (Fig. 2d). Then (H_a, K_a) corresponding to the amplitude maximum of the filtered stack (Fig. 2e and Supplementary Fig. 4d) are adopted as the updated estimate of (H_i, K_i) at site S_i . These updates are performed iteratively over all sites within the

map region.



Supplementary Figure S6 | Receiver function example for central Nevada site TA.O09A. **a**, Transverse receiver functions. Grey lines are EARS measurements from all 53 events, with time axis scaled to match the P_s arrival to that of a common zero ray parameter. The red line is a stack of all receiver functions, and blue is a synthetic receiver function using H and K from the final model (with assumed 10° angle of incidence, similarly time-scaled to zero ray parameter). **b**, Radial receiver functions.

Likelihood filters for this analysis do not force estimates to match the variogram and gravity constraints, but instead guide the model away from receiver function H - K stack maxima that result from interference with structural complexities. Supplementary Fig. 6 shows

observed receiver functions (time-scaled to remove dependence of P_s arrival time on ray parameter) for the 53 events recorded at site TA.O09A. These, and their stack, are compared to a synthetic receiver function generated for the simple Earth model ($H = 29.75$; $K = 1.76$) derived by our method, demonstrating that results reported here are consistent with the raw receiver function data.

30. Davis, J. C. *Statistics and Data Analysis in Geology* 2nd edn (Wiley, 1986).
31. Grieser, J., Gommers, R., Cofield, S. & Bernardi, M. Data sources for FAO worldmaps of Koeppen climatologies and climatic net primary production. http://www.fao.org/nr/climpag/globgrids/KC_commondata_en.asp (2006).
32. Seipold, U. Temperature dependence of thermal transport properties of crystalline rocks — a general law. *Tectonophysics* **291**, 161–171 (1998).

33. Bouhifd, M. A., Andrault, D., Fiquet, G. & Richet, P. Thermal expansion of forsterite up to the melting point. *Geophys. Res. Lett.* **23**, 1143–1146 (1996).
34. Turcotte, D. L. & Schubert, G. *Geodynamics* 2nd edn (Cambridge Univ. Press, 2002).
35. Mareschal, J. C., Cunningham, J. P. & Lowell, R. P. Downward continuation of heat flow data: method and examples from the western United States. *Geophysics* **50**, 846–851 (1985).
36. Christensen, N. I. & Mooney, W. D. Seismic velocity structure and composition of the continental crust: a global view. *J. Geophys. Res.* **100**, 9761–9788 (1995).
37. Heard, H. C. & Page, L. Elastic moduli, thermal expansion and inferred permeability of two granites to 350 °C and 55 megapascals. *J. Geophys. Res.* **87**, 9340–9348 (1982).
38. Afonso, J. C., Ranalli, G. & Fernández, M. Thermal expansivity and elastic properties of the lithospheric mantle: results from mineral physics of composites. *Phys. Earth Planet. Inter.* **149**, 279–306 (2005).
39. Pollack, H. N. On the use of the volumetric thermal expansion coefficient in models of ocean floor topography. *Tectonophysics* **64**, T45–T47 (1980).
40. Korenaga, J. Effective thermal expansivity of Maxwellian ocean lithosphere. *Earth Planet. Sci. Lett.* **257**, 343–349 (2007).
41. Erkan, K. & Blackwell, D. Transient thermal regimes in the Sierra Nevada and Baja California extinct outer arcs following the cessation of Farallon subduction. *J. Geophys. Res.* **114**, doi:10.1029/2007JB005498 (2009).
42. Dziewonski, A. M. & Anderson, D. L. Preliminary Reference Earth Model. *Phys. Earth Planet. Inter.* **25**, 297–356 (1981).
43. DeNosaquo, K. R., Smith, R. B. & Lowry, A. R. Density and lithospheric strength models of the Yellowstone-Snake River Plain volcanic system from gravity and heat flow data. *J. Volcanol. Geotherm. Res.* **188**, 108–127 (2009).
44. Yuan, H. Y., Dueker, K. & Stachnik, J. Crustal structure and thickness along the Yellowstone hot spot track: evidence for lower crustal outflow from beneath the eastern Snake River Plain. *Geochem. Geophys. Geosyst.* **11**, doi:10.1029/2009GC002787 (2010).
45. Beck, J. V. & Arnold, K. J. *Parameter Estimation in Engineering and Science* (Wiley, 1977).